Title

Quasi-monoenergetic and tunable x-rays from a laser-driven Compton light source

Authors

N. D. Powers, I. Ghebregziabher, G. Golovin, C. Liu, S. Chen, S. Banerjee, J. Zhang, and D. P. Umstadter*

Affiliations

Department of Physics and Astronomy, University of Nebraska-Lincoln, Lincoln 68588 USA

****Note:** This manuscript is the pre-print version (10/1/13 final submission) of an article published in Nature Photonics (doi:10.1038/nphoton.2013.314).

Introductory Paragraph

The maximum achievable photon energy of compact conventional Compton scattering x-ray light sources is currently limited by the maximum permissible field gradient of conventional electron accelerators[1, 2]. An alternate compact Compton x-ray source architecture with no such limitation is based instead on a high-field-gradient laser-wakefield accelerator[3-6]. In this case, a single high power (100-TW) laser system generates intense laser pulses used for both electron acceleration and scattering. While such all-laser-based sources have been demonstrated in proof-of-principle experiments to be bright and energetic[7-10], they have lacked until now several important distinguishing characteristics of conventional Compton sources. We now report the experimental demonstration of all-laser-driven Compton x-rays that are both quasi-monoenergetic

(~50% FWHM) and tunable (~70 keV to >1 MeV). These performance improvements are highly beneficial for several important x-ray radiological applications[2, 11-15].

Main Text

Synchrotron x-ray light sources are in use for scientific research worldwide, because of their high brightness, tunability, and narrow photon-energy bandwidth. However, synchrotrons are typically large devices (stadium-sized), due to the size of their component electron accelerator and undulator. More compact (room-sized) synchrotron x-ray sources were recently reported[1, 2], which use an electromagnetic undulator, operating on the principle of inverse-Compton scattering, instead of a fixed-magnet undulator. The much higher frequency of optical laser light used in Compton scattering, relative to fixed magnet arrays, reduces the electron energy required to produce x-rays, which in turn reduces the required size of the electron accelerator. Even greater size reduction can be achieved when laser light is used to drive both the undulator and the electron accelerator[7-10, 16].

The RF-cavity-driven accelerator at Lawrence Livermore National Laboratory (LLNL), produces 478-keV x-ray beams with 12% spectral bandwidth, 16-ps inferred temporal duration, and a flux of 10^5 photons/shot, corresponding to 1.5×10^{15} photons s^{-1} mm^{-2} $mrad^{-2}$ (per 0.1% bandwidth) peak brilliance. Utilizing a laser-wakefield accelerator (LWFA)[17, 18] with an accelerating field gradient >1,000x higher than conventional RF-cavity-driven accelerators, and thus is much more compact, we now demonstrate the production of quasi-monoenergetic x-rays that are 1,000x brighter with 10x more photons/shot. The increased brightness is due to the femtosecond pulse duration and micron-scale transverse size of LWFA *e*-beams and the x-rays they produce. This all-optical concept has been discussed theoretically[3-6, 19], and demonstrated in proof-of-

principle experiments[7-10]. However, the x-rays produced thus far have had large bandwidth and fixed energy, even though narrow-bandwidth and tunable LWFA-generated *e*-beams have already been demonstrated[20-25]. We now report x-rays from an LWFA-Compton light source that are not only bright and energetic, but also possess several other distinguishing characteristics of synchrotron light: narrow-bandwidth (~50% FWHM) and central energy tunability over a wide range (~70 keV to >1 MeV).

The experiment utilized the 100-TW, 800-nm *Diocles* laser at the University of Nebraska, Lincoln[26]. The laser beam is divided into two synchronized light pulses by an optical beam splitter. As shown schematically in Fig. 1a, one pulse drives the LWFA, and the other acts as an undulator, by scattering from the electrons (see Methods). After interacting with the laser pulse, the *e*-beam is swept out of the x-ray path by a dipole magnet, and onto a charge-calibrated detector, which records the *e*-beam energy spectrum and angular divergence for each shot (Fig. 1b). The transverse spatial profile of the forward-directed x-ray beam is recorded by a calibrated detector, Fig. 1c, placed outside of the vacuum system.

The x-ray spectral bandwidth was directly measured by comparing the x-ray transmittances through a set of four Ross-filter[27] pairs, with each pair composed of two elements of similar atomic number. The thickness of each pair (see Table 1) was designed such that the transmission curves closely match for all photon energies outside of the two *K* edges. The difference in transmitted signal through each pair (see Supplementary Fig. S1) was used to determine the number of photons with energies between the *K* edges (see Methods). The filters were arranged in a checkerboard pattern

to allow accurate reconstruction of the unfiltered x-ray spatial profile and to allow for multiple measurements across the beam's profile. Figure 2 shows the x-ray energy distribution, measured using filters contained within 4.5 mrad of the beam center [slightly smaller than the 10-mrad full width at half maximum (FWHM) beam divergence]. The x-ray spectrum was centered at 66 ± 7 keV, with an energy spread of ~50% FWHM (fitted using a Gaussian profile). By virtue of being peaked, rather than exponentially decaying with increasing energy (as in previous all-laser-driven Compton experiments[7-10]), this spectrum has the advantage of far fewer low-energy photons.

Assuming a collimated *e*-beam and narrow-bandwidth counter-propagating laser, the fractional bandwidth of the on-axis Compton-scattered spectrum is $\Delta E_\gamma/E_\gamma \approx 2\,\Delta E_e/E_e$, where E_e and ΔE_e are the *e*-beam average energy and energy spread, and E_γ and ΔE_γ are the x-ray beam average energy and energy spread, respectively. The measured *e*-beam spectrum is peaked at 55 ± 3 MeV, see Fig. 2 (inset), with a 22% (FWHM) energy spread (the spectral shape was well represented by a Gaussian fit) and 23-pC beam charge. The ~6% increase in the measured x-ray energy spread (~50%), as compared with the analytical prediction (~44%), is attributable to contributions from laser spectral bandwidth, scattering angle, divergence, and laser ponderomotive force, all of which in our case were small in comparison to the energy width contributed by the *e*-beam.

The experimental measurement of the x-ray bandwidth was compared with the predictions of a previously benchmarked numerical model[6] (see Supplementary Methods). The model simulated the scattered x-ray spectrum from the measured *e*-beam

characteristics (*i.e.*, the energy spectrum and energy-dependent divergence of Fig. 1b), represented by a six-dimensional phase space distribution, and the laser parameters (150-fs laser scattering pulse duration, focused intensity of 2×10^{17} W/cm^2). The model predicts an on-axis x-ray spectrum peaked at 71 keV. Off-axis, the x-ray central energy decreases smoothly with increasing polar angle. Averaging the spectrum over the polar angles measured in the experiment results in an additional red-shift, with no significant change in the spectral width. The simulated spectrum, including contributions from all photons within the area used for Ross-filter analysis, predicts an averaged spectrum (see Fig. 2) that peaks at 64 keV, with 50% fractional bandwidth. Thus, the energy, the bandwidth, and the number of photons within the measured region ($4.6\text{x}10^5$ simulated compared to $3\text{x}10^5$ measured) are all well within the uncertainty of the measurement.

The central x-ray energy was tuned over one order-of-magnitude by tuning the energy of the LWFA *e*-beams from ~50-300 MeV (see Fig. 3). A different filter set and analysis method (see Methods) were required to measure the x-ray photon energy over this much larger range, due to limited working-range of the Ross-filter technique (see Supplementary Fig. S2). While the central energy could be measured by this method, the energy spread could not. For the ~70 shots in which the x-ray energy could be analyzed, the average x-ray central energy is observed to follow a quadratic scaling with the average *e*-beam central energy, as the latter was tuned. This agrees with the theoretically predicted $E_\gamma = 4\gamma^2 E_L$ scaling for photons backscattered on-axis by a single electron, where E_L and E_γ are the scattering laser and scattered x-ray photon energies, respectively, and γ is the relativistic Lorentz factor of the electron.

The reproducibility and stability of the x-rays were also computed, but using a larger data set. X-ray beams were observed on >93% of shots (664 in total) when the scattering beam was present, illustrating the reproducibility of x-ray generation. For 56% of these shots, quasi-monoenergetic *e*-beams (energy spread $\lesssim$25%) were measured. From the above experimental results and theoretical analysis, we can infer that the x-rays on these shots were also quasi-monoenergetic (energy spread $\lesssim$50%). The measured electron energy spread, and thus inferred x-ray energy spread, was found to be the most stable for the lowest and highest electron energy settings, where >74% of the beams were quasi-monoenergetic (see Supplementary Fig. S3).

The x-ray photon number was stable to within 60% of its average value, 1.7×10^6 (see Supplementary Fig. S4). The photon number, and thus photon flux, depends on three factors: scattering-laser beam intensity, degree of beam overlap, and *e*-beam charge. The stability was dominated by the stability of the *e*-beam charge which for this data set was stable to within 45% of its average value, 29 pC. Greater control of the flux can be achieved by stabilizing the *e*-beam charge and adjusting the scattering-beam intensity.

The all-laser-driven architecture has several advantages. Besides a small overall device size, the electron and scattering beam parameters are also well matched in size, and the pulses are well synchronized. These characteristics lead to high peak x-ray brightness: ~ 3×10^{18} photons s^{-1} mm^{-2} $mrad^{-2}$ (per 0.1% bandwidth) for 70-keV beams from Fig. 2, and ~10^{19} for 1-MeV beams from Fig. 3. The brightness was calculated using the measured beam divergence and photon number, and assuming a 30-fs x-ray pulse duration and 6-

μm (rms) x-ray source size[10]. The 1-MeV beam brightness is comparable to previously reported polychromatic x-ray beams of similar energy[10].

The improved x-ray characteristics reported here should expand the reach of compact all-laser-driven Compton x-ray sources. For instance, narrow x-ray bandwidth, relative to bremsstrahlung, significantly reduces the amount of unwanted radiation in medical imaging. Consequently, radiographic image quality is improved[12], patient risk is decreased[11, 13], and beam-hardening effects are reduced[2]. Additionally, photon energy-tunability can enhance radiographic imaging[12].

Further improvements in x-ray performance can be expected, by incorporating techniques used in conventional Compton sources and/or advances in LWFA technology. For instance, by using either higher scattering photon energy (achieved by harmonic conversion) or higher LWFA electron energy[25, 28], the x-ray energy will soon exceed the threshold for nuclear photo-disintegration (~10 MeV)[14, 15]. Similarly, lower-bandwidth x-rays will result from using lower-bandwidth *e*-beams[20-23]. Finally, the control and stability of the x-ray energy will be substantially improved by recent advances in the degree of control and stability achieved for LWFA electron energy[24].

Methods Summary

Laser. The drive beam was operated from 1.3-1.7 J. Spectral- and spatial-phase correction optimized the beam characteristics[26]. The resulting 33-fs pulse was focused, with an f/14 parabolic mirror, to a 21-μm (FWHM) Gaussian focal spot. The 150-fs, 130-

170-mJ scattering beam was focused, with a thin positive lens (f=1000 mm), to 17 μm (FWHM).

Undulator parameters. The *e*-beam and scattering laser were spatio-temporally overlapped 1.5 mm downstream of the accelerator exit at a 170-degree angle (nearly backscattering). The laser had N = 56 cycles, and strength parameter of a_0 = 0.3.

Accelerator parameters. We used a dual-stage gas jet accelerator consisting of an injector stage of a 99:1 He:N_2 mixed gas mixture[29, 30], and an accelerator stage of pure He. The central energy was increased, within a given range, by increasing the plasma density of the accelerator stage. Using a longer accelerator stage shifted the tunable energy range higher. The plasma density of the 0.5-mm acceleration stage was scanned from $2x10^{17}$-$2x10^{18}$ cm^{-3}. For the two highest energy data points shown in Fig. 3, a 2-mm acceleration stage density was scanned from $1.2x10^{18}$-$1.7x10^{18}$ cm^{-3}. A future publication will provide further details on the accelerator.

Detection. The electron spectrometer consisted of a 19-cm, 0.8-T magnet and a Gd_2O_2S:Tb screen (LANEX) imaged by a 12-bit CCD camera. A magnetic field map was used to calculate the electron deflection versus energy. The LANEX was placed outside of the x-ray beam path to allow simultaneous measurement of the x-rays and electrons.

The x-ray detector was a 40x40-voxel array of 1-mm square, 1-cm deep cesium iodide (CsI) crystals imaged by a 14-bit EMCCD camera. All voxels were separated by a 0.2-mm wide epoxy. Cross-talk between voxels was measured using an x-ray tube source.

X-ray spectral measurement (Ross filters). Each filter was cut into a 1.2-mm square, and aligned to a single detector voxel. The x-ray beam profile in filtered regions was reconstructed by a 2-D bi-harmonic spline interpolation. A transmittance map was produced by dividing the measured signal by the reconstructed one.

The signal difference between two filters of a Ross-pair was used to calculate the number of photons within the measurement bandwidth of the pair (ΔE), written explicitly as $\Delta S = \int_0^\infty X(E)\Omega(E)\Delta T(E)dE$, where E is photon energy, $\Omega(E)$ is the detector response, and S and T are the signal level and transmittance of individual filters, respectively. Assuming the x-ray photon density has a nearly linear slope within each Ross-pair bandwidth, the photon density can be written as $X(E) = X^{\mathrm{avg}}[1 + \beta\,(E - E^{\mathrm{avg}})/\Delta E]$, where E^{avg} is the average energy within the bandwidth and β is the slope of the distribution within the bandwidth. The average photon density, $X^{\mathrm{avg}} = \Delta S/\int_{E_1}^{E_2}[1 + \beta\,(E - E^{\mathrm{avg}})/\Delta E]\Omega(E)\Delta T(E)dE$, is obtained by integrating across the Ross-pair bandwidth. We used $\beta = 0$ to calculate the x-ray photon density, but included uncertainty in the slope in the error analysis as $\sigma_\beta = \left|X^{\mathrm{avg}}_{\beta=\beta_{\max}} - X^{\mathrm{avg}}_{\beta=-\beta_{\max}}\right|/X^{\mathrm{avg}}_{\beta=0}$. The upper limit of the slope ($\beta_{\max} = 4$) was estimated from simulations. Other factors contributing to the error bars include: uncertainty in filter thickness, cross-talk between voxels, and filter bandgap leakage. Measurements of a polychromatic and a higher energy beam are shown in Supplementary Fig. S2, demonstrating the response of this technique to different spectral distributions.

Energy scaling analysis (continuum-attenuation filters). The central x-ray energy was measured with various broadband transmission filters (instead of *K* edge filters from the Ross technique), including: 1.6-, 3-, and 12-mm aluminum, 0.5-, 1-, 1.5-, 2-, 3-, 4.5-, and 6-mm copper, 1.6-mm lead, and 0.175-mm uranium. The two highest energy data points used 6.25-mm aluminum, 1.52-mm copper, and 6.24-mm lead. The filter edges were aligned across voxel rows and/or columns, with >2 voxels between neighboring filters, in crisscrossed-strip-filter, quad-filter, or step-filter arrangements.

Shot-to-shot fluctuation in beam centering on the filters limited the number of shots that could be analyzed. Since beam energy and pointing are not correlated, no bias was introduced by analyzing this subset of shots. The central energy of quasi-monoenergetic x-ray beams (<25% energy spread in the corresponding *e*-beam) was analyzed only if the x-rays were centered on the appropriate filter set; thus, providing adequate signal-to-noise ratio for accurate profile reconstruction.

The beam profile in filtered regions was reconstructed by 2-D Gaussian fitting. The measured transmissions for each shot were compared to simulated transmissions for all combinations of x-ray central energy and energy spread; each combination represented a single test spectrum. The x-ray central energy and measurement uncertainty are determined from the set of test spectra with transmission values within the measurement error and a bandwidth <150% of the analytical prediction. Some knowledge of the x-ray spectral shape, determined from the measured *e*-beam energy distribution, was required to determine the central energy. Methodological consistency for all data points ensured

accurate representation of the energy scaling. Only a lower limit of the central energy was determined for the two highest energy sets.

References

1. Albert, F. *et al*. Characterization and applications of a tunable, laser-based, MeV-class Compton-scattering gamma-ray source. *Phys. Rev. ST Accel. Beams* **13,** 070704 (2010).

2. Achterhold, K. *et al*. Monochromatic computed tomography with a compact laser-driven X-ray source. *Scientific Reports* **3,** 1313 (2013).

3. Catravas, P., Esarey, E. & Leemans, W. P. Femtosecond x-rays from Thomson scattering using laser wakefield accelerators. *Meas. Sci. Technol.* **12,** 1828-1834 (2001).

4. Umstadter D., He F., & Lau Y. U.S. Patent No. 7,321,604. (2008).

5. Esarey, E., Schroeder, C. B. & Leemans, W. P. Physics of laser-driven plasma-based electron accelerators. *Rev. Mod. Phys.* **81,** 1229-1285 (2009).

6. Ghebregziabher, I., Shadwick, B. A. & Umstadter, D. Spectral bandwidth reduction of Thomson scattered light by pulse chirping. *Phys. Rev. ST Accel. Beams* **16,** 030705 (2013).

7. Schwoerer, H., Liesfeld, B., Schlenvoigt, H. P., Amthor, K. U. & Sauerbrey, R. Thomson-backscattered X rays from laser-accelerated electrons. *Phys. Rev. Lett.* **96,** 014802 (2006).

8. Ta Phuoc, K. *et al*. All-optical Compton gamma-ray source. *Nat. Photonics* **6,** 308-311 (2012).

9. Mori, Y. *et al*. Head-on inverse Compton scattering X-rays with energy beyond 10 keV from laser-accelerated quasi-monoenergetic electron bunches. *Appl. Phys. Expr.* **5,** 056401 (2012).

10. Chen, S. *et al*. MeV-energy X Rays from inverse Compton scattering with laser-wakefield accelerated electrons. *Phys. Rev. Lett.* **110,** 155003 (2013).

11. Boone, J. M. & Seibert, J. A. A figure of merit comparison between bremsstrahlung and monoenergetic X-ray sources for angiography. *J. X-Ray Sci. Technol.* **4,** 334-345 (1994).

12. Carroll, F. E. Tunable monochromatic X Rays: A new paradigm in medicine. *Am. J. Roentgenol.* **179,** 583-590 (2002).

13. Brenner, D. J. *et al*. Cancer risks attributable to low doses of ionizing radiation: Assessing what we really know. *Proc. Natl. Acad. Sci. U S A* **100,** 13761-13766 (2003).

14. Giulietti, A. *et al*. Intense γ-ray source in the giant-dipole-resonance range driven by 10-TW laser pulses. *Phys. Rev. Lett.* **101,** 105002 (2008).

15. Habs, D. *et al*. Vision of nuclear physics with photo-nuclear reactions by laser-driven gamma beams. *Eur. Phys. J. D* **55,** 279-285 (2009).

16. Corde, S. *et al*. Femtosecond X rays from laser-plasma accelerators. *Rev. Mod. Phys.* **85,** 1-48 (2013).

17. Tajima, T. & Dawson, J. M. Laser electron accelerator. *Phys. Rev. Lett.* **43,** 267-270 (1979).

18. Esarey, E., Ride, S. K. & Sprangle, P. Nonlinear Thomson scattering of intense laser pulses from beams and plasmas. *Phys Rev E.* **48,** 3003-3021 (1993).

19. Hartemann, F. V. *et al*. Compton scattering X-ray sources driven by laser wakefield acceleration. *Phys. Rev. ST Accel. Beams* **10,** 011301 (2007).

20. Geddes, C. G. R. *et al*. High-quality electron beams from a laser wakefield accelerator using plasma-channel guiding. *Nature* **431,** 538-541 (2004).

21. Mangles, S. P. D. *et al*. Monoenergetic beams of relativistic electrons from intense laser-plasma interactions. *Nature* **431,** 535-538 (2004).

22. Faure, J. *et al*. A laser-plasma accelerator producing monoenergetic electron beams. *Nature* **431,** 541-544 (2004).

23. Brunetti, E. *et al*. Low emittance, high brilliance relativistic electron beams from a laser-plasma accelerator. *Phys. Rev. Lett.* **105,** 215007 (2010).

24. Gonsalves, A. J. *et al*. Tunable laser plasma accelerator based on longitudinal density tailoring. *Nat Phys* **7,** 862-866 (2011).

25. Banerjee, S. *et al*. Generation of tunable, 100-800 MeV quasi-monoenergetic electron beams from a laser-wakefield accelerator in the blowout regime. *Phys. Plasmas* **19,** 056703 (2012).

26. Liu, C. *et al*. Repetitive petawatt-class laser with near-diffraction-limited focal spot and transform-limited pulse duration. *Proc. SPIE 8599, Solid State Lasers XXII: Technology and Devices*, 859919 (2013).

27. Ross, P. A. A new method of spectroscopy for faint X-radiations. *J. Opt. Soc. Am.* **16,** 433-436 (1928).

28. Leemans, W. P. GeV electron beams from a centimetre-scale accelerator. *Nat. Phys.* **2,** 696-699 (2006).

29. Liu, J. S. *et al*. All-optical cascaded laser wakefield accelerator using ionization-induced injection. *Phys. Rev. Lett.* **107,** 035001 (2011).

30. Pollock, B. B. *et al*. Demonstration of a narrow energy spread, similar to 0.5 GeV electron beam from a two-stage laser wakefield accelerator. *Phys. Rev. Lett.* **107,** 045001 (2011).

Acknowledgments We thank K. Brown, J. Mills, and C. Petersen for their contributions to the laser facility. We thank D. Haden and N. Cunningham from Nebraska Wesleyan University for their contributions with x-ray detector analysis. We thank C. Wilson, T. Anderson and D. Alexander from the University of Nebraska-Lincoln Electrical Engineering department for precision cutting of Ross filters. This material is based upon work supported by U.S. Department of Energy: DE-FG02-05ER15663, Defense Threat Reduction Agency: HDTRA1-11-C-0001, Air Force Office for Scientific Research: FA 9550-08-1-0232, and FA9550-11-1-0157, Department of Homeland Security: 2007-DN-077-ER0007-02, Defense Advanced Research Projects Agency: FA9550-09-1-0009 and USSTRATCOM: FA4600-12-D-9000. The views expressed here do not represent those of the sponsors.

Author Contributions Conception and design: DP, NP, SB, SC, IG, CL, GG; Experiments: GG, NP, SB, SC, IG, CL, JZ; Data analysis: GG, IG, NP; Materials / analysis tools: GG, IG, SB, NP; Writing: DP, NP.

Competing financial interests The authors declare no competing financial interests.

Author Information Reprints and permissions information is available at www.nature.com/reprints. Correspondence and requests for materials should be addressed to donald.umstadter@unl.edu.

Figure Legends

Figure 1: X-ray generation and detection. (a) Experimental setup (not to scale). Electrons (green) are accelerated by the interaction of a drive laser beam (red, from left to right) with a plasma created within the plume of a dual-stage gas jet, and then deflected to a LANEX screen. A second laser pulse (red, from right to left) scatters from the *e*-beam after the accelerator. The x-ray beam (purple) is recorded by a CsI detector after passing through Ross filters arranged in a checkerboard pattern. **(b)** Raw LANEX image of electron beam spectrum. **c)** Processed x-ray profile imaged through Ross filters.

Figure 2: X-ray bandwidth measurement. X-ray spectral distribution (■) measured, for a single shot, by the Ross-filter pairs. Horizontal error bars represent the spectral width of the filter pair, and vertical error bars represent the measurement error, including: uncertainty in filter thickness, cross-talk between voxels, and filter bandgap leakage. The

simulated x-ray spectrum (—), obtained from experimentally measured *e*-beam spectrum (inset), is normalized by dividing by a factor of 1.4.

Figure 3: X-ray energy tuning. (a) The measured x-ray central energy, plotted versus the measured *e*-beam central energy, is consistent with a $4\gamma^2$ scaling (— — —). The same data set, plotted versus plasma density (inset), illustrates that the *e*-beam energy was controlled by adjusting the plasma density of two separate accelerator jets. For a given accelerator-jet length (0.5-mm (■) and 2-mm (▲)), the plasma density of the injector-jet was fixed (1.7×10^{18} cm^{-3} and 2.9×10^{18} cm^{-3}, respectively). Each point is the average of, from left to right, 25, 8, 8, 3, 5, 7, 8, and 5 selected shots (see Methods) taken with the same gas-jet parameters. Error bars represent 80% confidence intervals, calculated using the *t*-distribution of measurements of the set. **(b)** Individual *e*-beam spectra from this data set were chosen to best represent the average *e*-beam energy of the set. The beams are quasi-monoenergetic across the entire tunable range.

Tables

Ross pair	Filter 1	Filter 2
1	Dy (96 ± 1 μm) Cu (50 ± 1 μm)	Sn (234 ± 2 μm) Cu (25 ± 1 μm)
2	Ta (41± 1 μm) Cu (16 ± 1 μm)	Dy (96 ± 1 μm) Cu (50 ± 1 μm)
3	Au (30 ± 1 μm um) Cu (6 ± 1 μm um)	Ta (41 ± 1 μm) Cu (16 ± 1 μm)
4	Pb (48 ± 1 μm)	Au (30 ± 1 μm) Cu (6 ± 1 μm)

Table 1: Ross-filter pairs used for x-ray spectral measurement. Errors represent the sum of both measurement errors, determined from device sensitivity, and variation in filter thickness across the sample.

Fig. 1

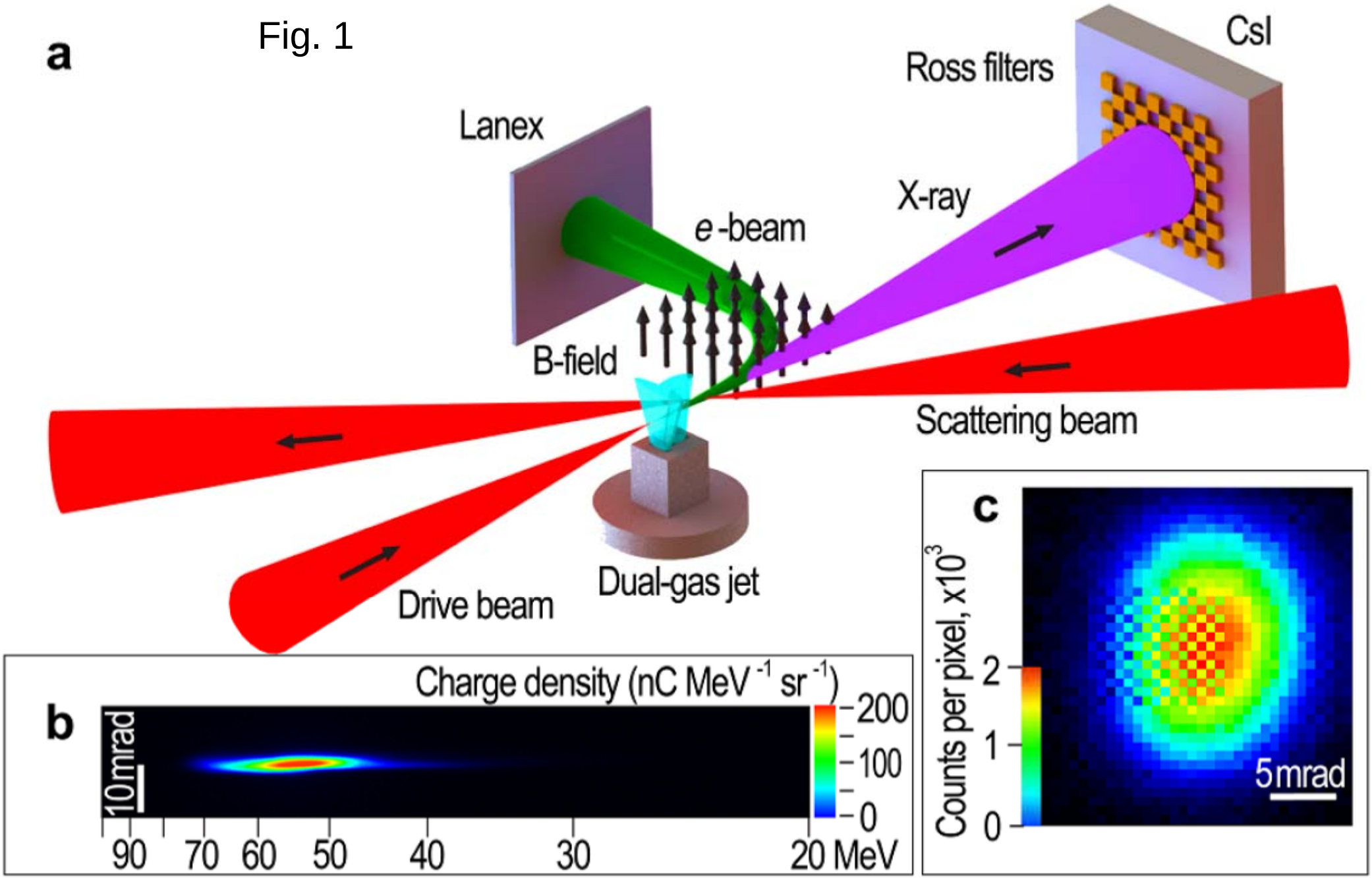
a
CsI
Ross filters
Lanex
X-ray
e -beam
B-field
Scattering beam
Drive beam
Dual-gas jet
b
Charge density (nC MeV -1 sr -1)
10mrad
200
100
0
90
70
60
50
40
30
20 MeV
c
Counts per pixel, x10^3
2
1
0
5mrad

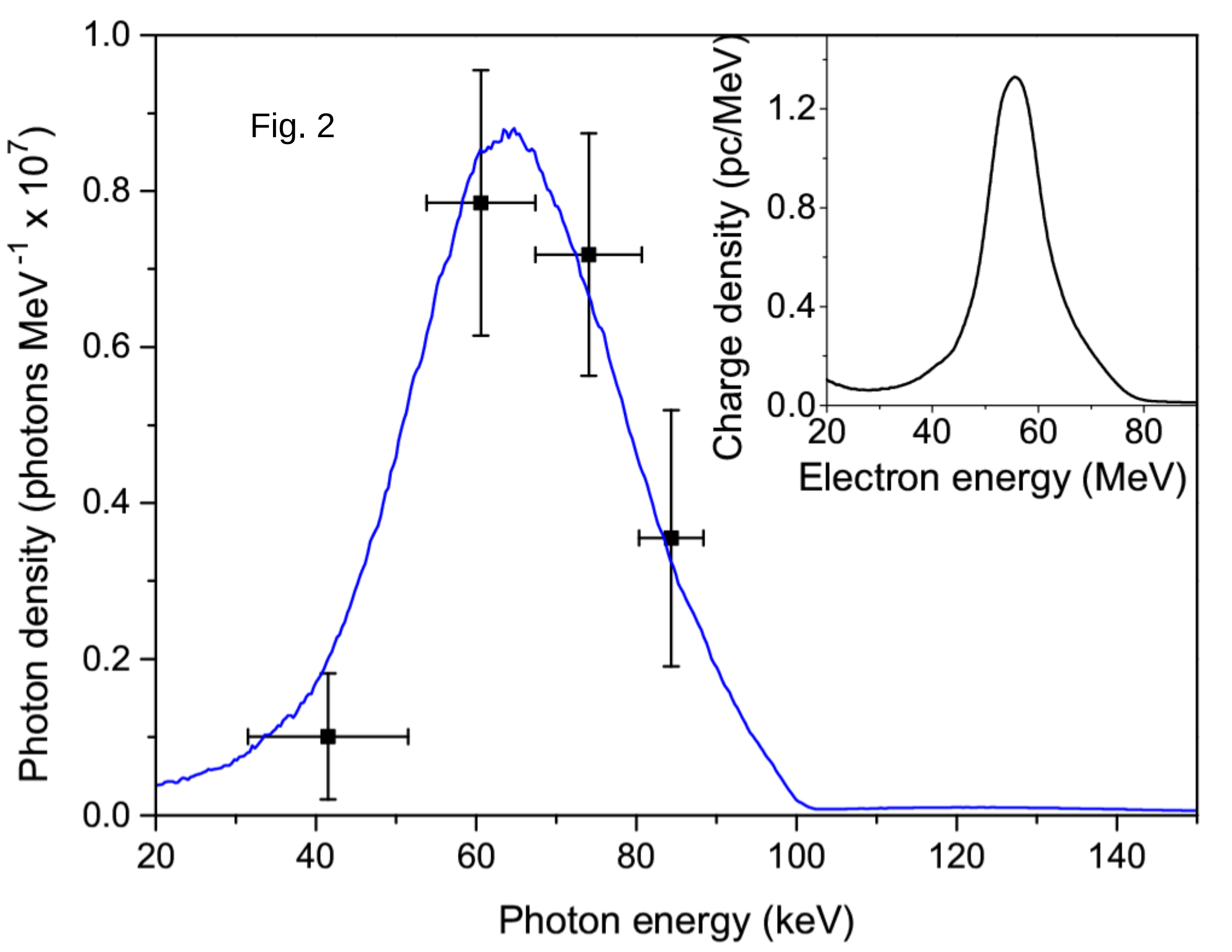
Fig. 2
Photon density (photons MeV^{-1} x 10^{7})
Photon energy (keV)
1.0
0.8
0.6
0.4
0.2
0.0
20
40
60
80
100
120
140
Charge density (pc/MeV)
Electron energy (MeV)
1.2
0.8
0.4
0.0
20
40
60
80

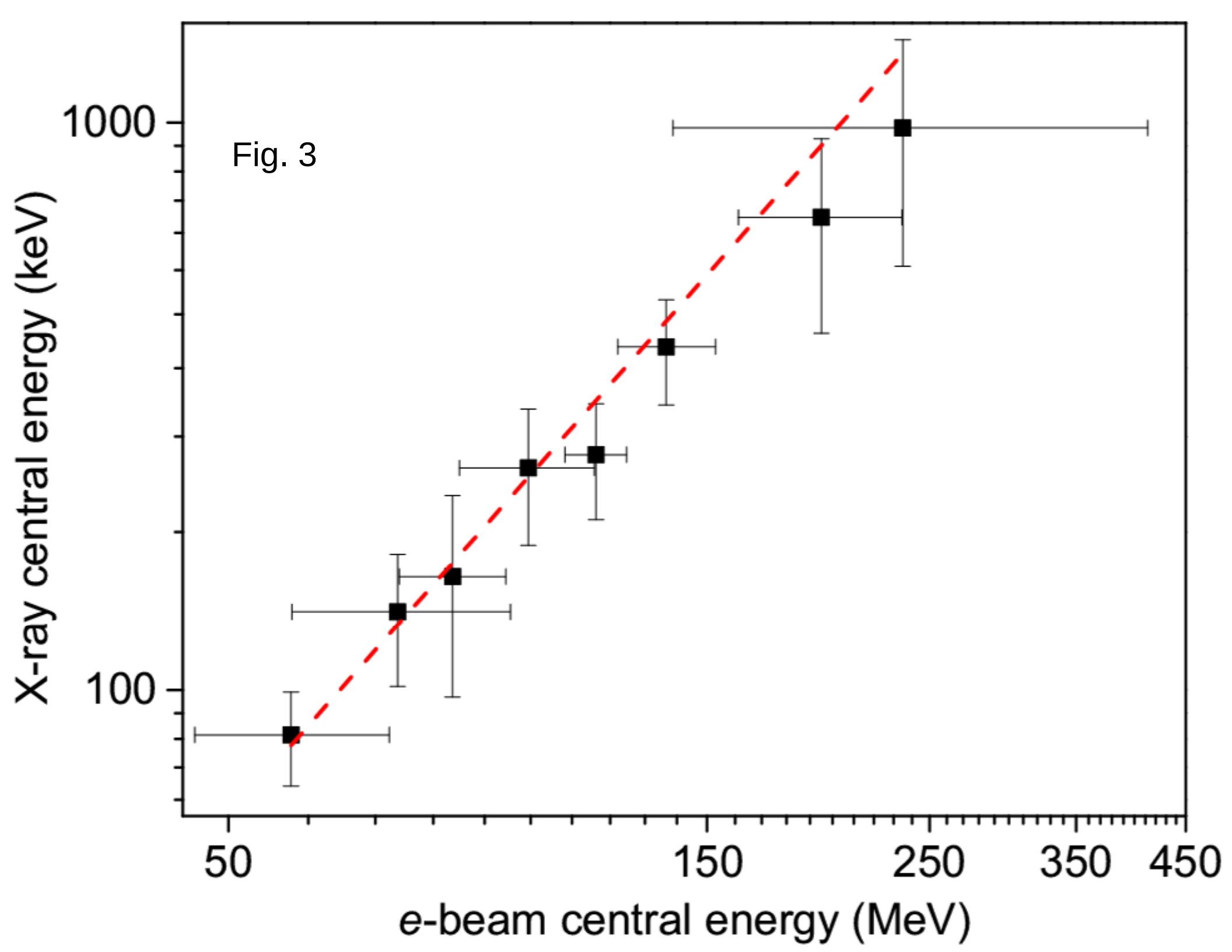
Fig. 3
1000
100
X-ray central energy (keV)
50
150
250
350
450
e-beam central energy (MeV)

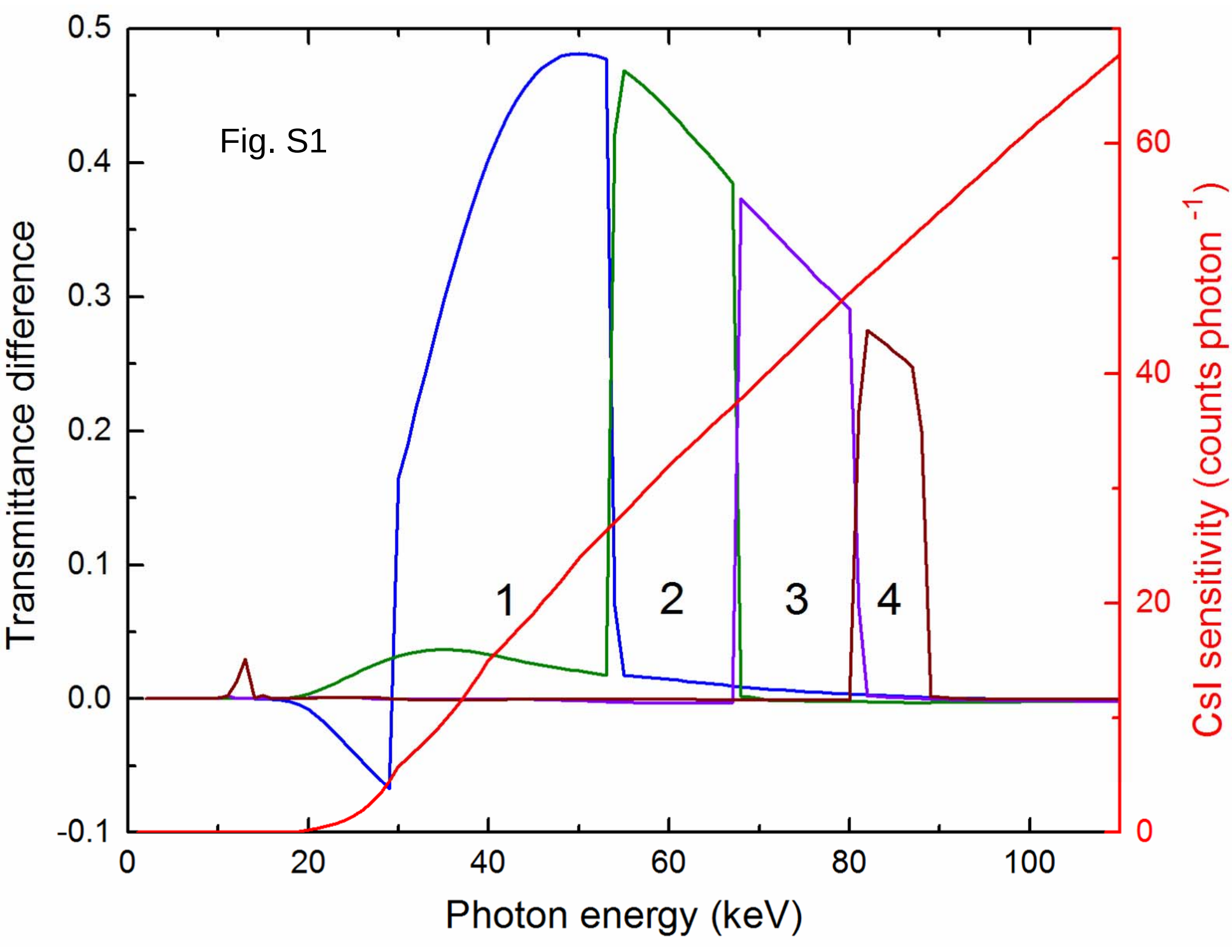
Fig. S1
Transmittance difference
CsI sensitivity (counts photon^{-1})
Photon energy (keV)
0.5
0.4
0.3
0.2
0.1
0.0
-0.1
0
20
40
60
80
100
1
2
3
4

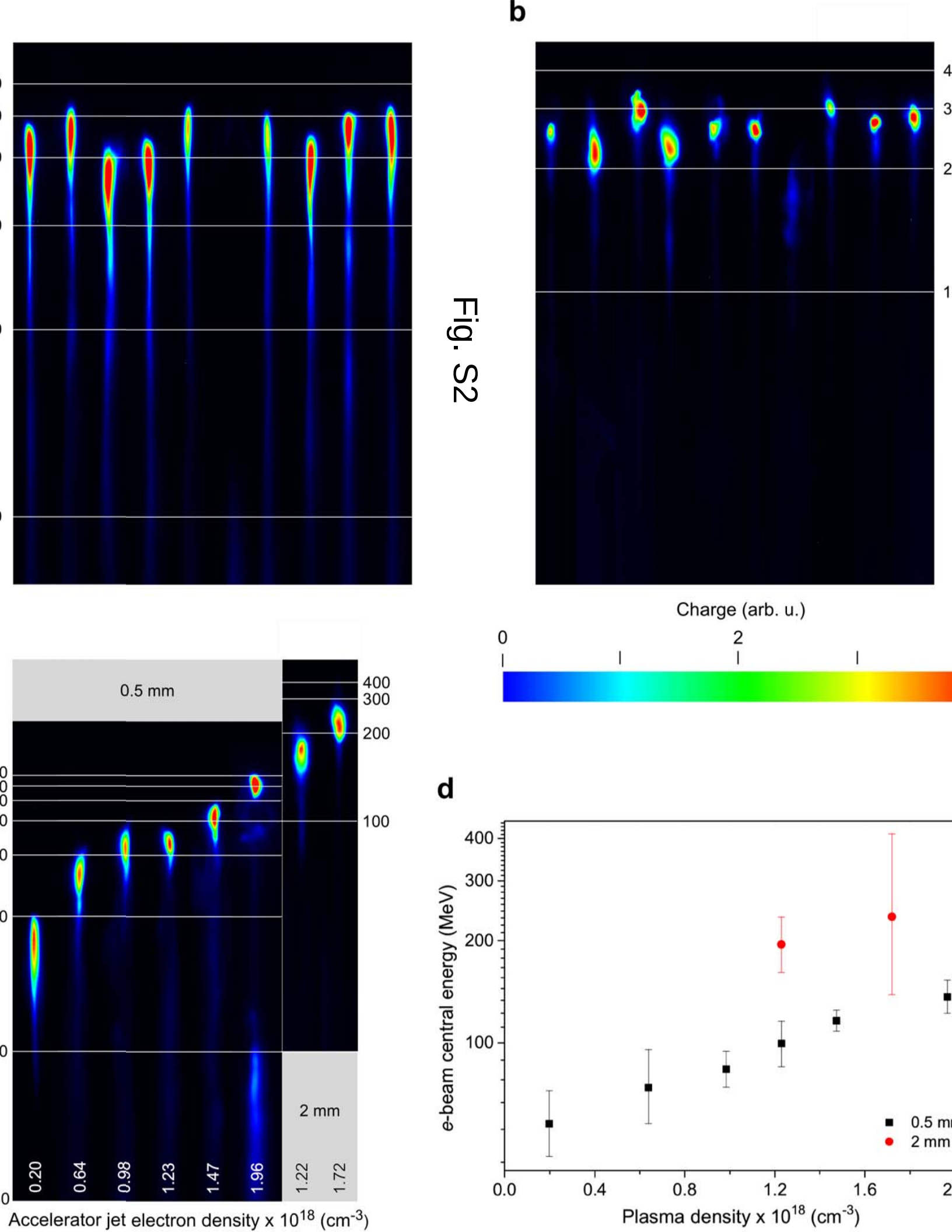
b
Charge (arb. u.)
0
2
0.5 mm
2 mm
400
300
200
100
0.20
0.64
0.98
1.23
1.47
1.96
1.22
1.72
Accelerator jet electron density x 10^18 (cm^-3)
d
e-beam central energy (MeV)
Plasma density x 10^18 (cm^-3)
0.0
0.4
0.8
1.2
1.6
0.5 mm
2 mm

Fig. S2

Fig. S3

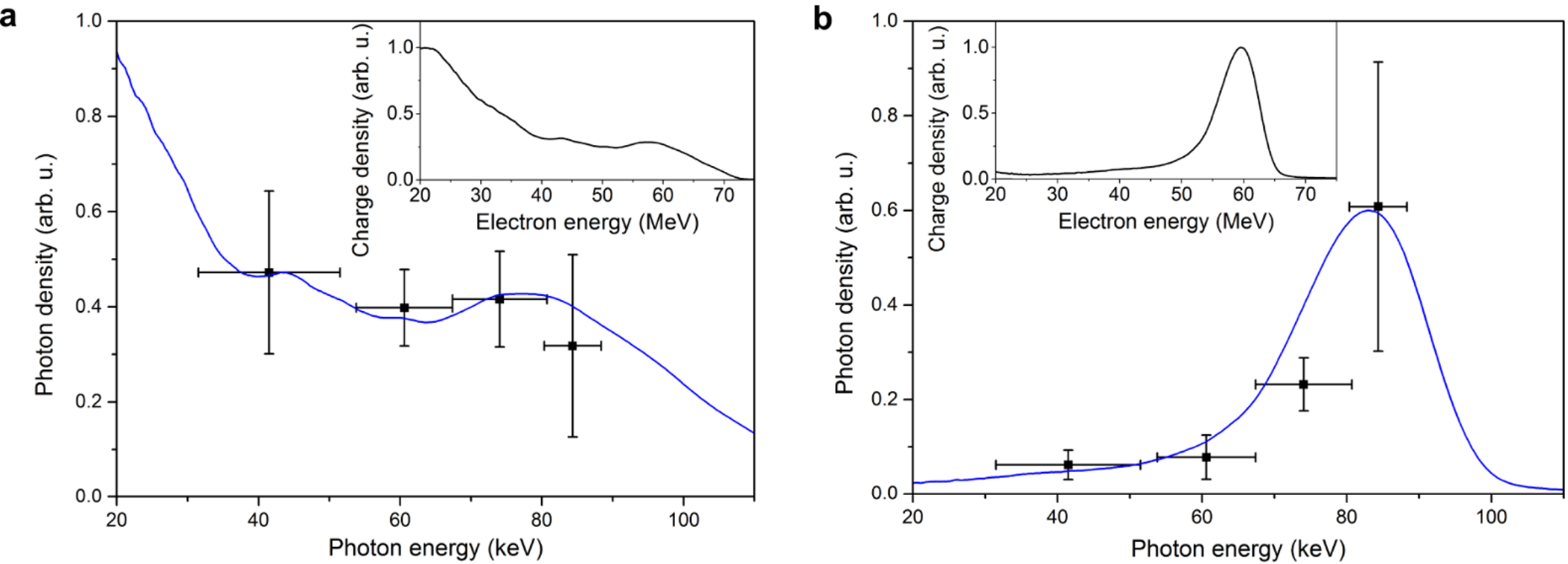
a
Photon density (arb. u.)
Photon energy (keV)
Charge density (arb. u.)
Electron energy (MeV)
b
Photon density (arb. u.)
Photon energy (keV)
Charge density (arb. u.)
Electron energy (MeV)

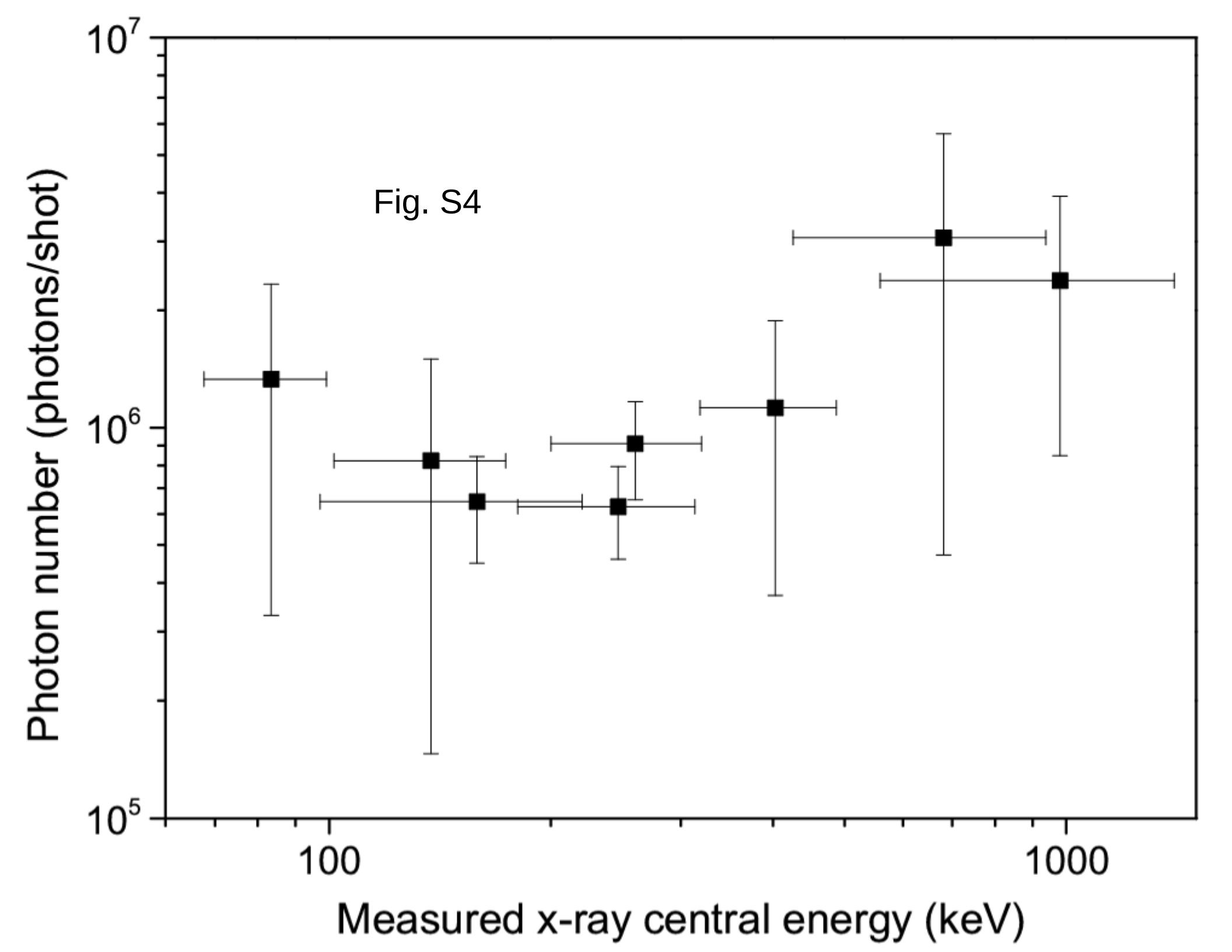
Fig. S4
Photon number (photons/shot)
10^7
10^6
10^5
100
1000
Measured x-ray central energy (keV)